ACS OMEGA

http://pubs.acs.org/journal/acsodf

Article

Charge Compensation Mechanisms and Oxygen Vacancy Formations in $LiNi_{1/3}Co_{1/3}Mn_{1/3}O_2$: First-Principles Calculations

Xiao-Hong Shi, Ya-Ping Wang, Xinrui Cao, Shunqing Wu, Zhufeng Hou, and Zizhong Zhu*

Cite This: *ACS Omega* 2022, 7, 14875−14886

Read Online

ACCESS | Metrics & More | Article Recommendations

ABSTRACT: Charge compensation mechanisms in the delithiation processes of $LiNi_{1/3}Co_{1/3}Mn_{1/3}O_2$ (NCM111) are compared in detail by the first-principles calculations with GGA and GGA+U methods under different U values reported in the literature. The calculations suggested that different sets of U values lead to different charge compensation mechanisms in the delithiation process. Co^{3+}/Co^{4+} couples were shown to dominate the redox reaction for $1 \geq x \geq 2/3$ by using the GGA+U_1 method (U_1 = 6.0 3.4 3.9 for Ni, Co, and Mn, respectively). However, by using the GGA+U_2 (U_2 = 6.0 5.5 4.2) method, the results indicated that the redox reaction of Ni^{2+}/Ni^{3+} took place in the range of $1 \geq x \geq 2/3$. Therefore, according to our study, experimental charge compensation processes during delithiation are of great importance to evaluate the theoretical calculations. The results also indicated that all the GGA+U_i (i = 1, 2, 3) schemes predicted better voltage platforms than the GGA method. The oxygen anionic redox reactions during delithiation are also compared with GGA+U calculations under different U values. The electronic density of states and magnetic moments of transition metals have been employed to illustrate the redox reactions during the lithium extractions in NCM111. We have also investigated the formation energies of an oxygen vacancy in NCM111 under different values of U, which is important in understanding the possible occurrence of oxygen release. The formation energy of an O vacancy is essentially dependent on the experimental conditions. As expected, the decreased temperature and increased oxygen partial pressure can suppress the formation of the oxygen vacancy. The calculations can help improve the stability of the lattice oxygen.

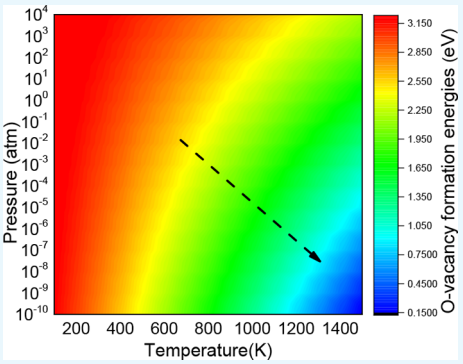

1. INTRODUCTION

Rechargeable lithium-ion batteries have entered the electrical vehicle market and plug-in hybrid vehicles because of their high energy density, high working voltage, long cycle life, outstanding safety characteristics, and environmental friendliness.[1,2] Although lithium transition metal (TM) oxides such as layered structured material $LiCoO_2$[3−10] and olivine structured materials $LiFePO_4$[11−17] are good cathode materials for lithium-ion batteries, cobalt is relatively costly while $LiFePO_4$ has a low energy storage capability. Hence, great efforts have been made to reduce the Co content in $LiCoO_2$ material; therefore, the layered $LiNi_{1/3}Co_{1/3}Mn_{1/3}O_2$ (NCM111)[18−27] is one of the most studied systems. Although NCM111 has been studied extensively, the available results are not considered to be sufficient to regard the problem as completely solved. For example, the electrochemical properties dependent on U are not well understood, as the GGA+U method is very necessary to describe the strong electron correlations of d-orbitals of the transition metal elements.[28] In this work, the electrochemical properties and the formation energy of an oxygen vacancy in NCM111 cathode material have been investigated by first-principles calculations. In particular, charge compensation mechanisms during delithiation in NCM111 are compared in detail with GGA and GGA+U calculations under different U values reported in the literature. The calculations suggest that different sets of U values lead to different charge compensation mechanisms in the delithiation process. Therefore, experimental charge compensation processes during delithiation are then of great importance to evaluate the theoretical calculations, although theoretical calculations are declared as *ab initio*. The oxygen anionic redox reactions during delithiation are also compared by using GGA+U calculations under different U values. Furthermore, the results also indicated that all the GGA+U_i (i = 1, 2, 3) schemes predicted better voltage platforms than the GGA method.

The formation of oxygen vacancies could affect various properties of the host oxide cathode materials, such as the cycling stability in the batteries.[10] The understanding of the behavior of oxygen vacancies in oxides becomes important and

Received: January 19, 2022
Accepted: April 12, 2022
Published: April 19, 2022

can help lay the foundation for the anion defect engineering to boost the electrochemical performance of cathode materials. In this paper, we have also investigated the formation energies of an oxygen vacancy in the bulk phase of NCM111, which could help understand the possible occurrence of the oxygen vacancy. These calculations can also provide guidelines for reducing the oxygen release and improving the stability of the lattice oxygen in the cathode materials of the lithium-ion batteries. The formation energy of an O vacancy is essentially dependent on the experimental conditions. As expected, the increased temperature and decreased oxygen partial pressure decrease the formation energy of the O vacancy; that is, the lower temperature and higher oxygen partial pressure can suppress the formation of the oxygen vacancy.

2. CALCULATION METHODS

All the calculations have been performed by using the Vienna *ab initio* simulation package (VASP), which is based on the density functional theory (DFT), the plane wave basis, and the projector augmented wave (PAW) representation.[29,30] The Perdew−Burke−Ernzerhof (PBE) functional for the generalized gradient approximation (GGA) is used to process the electron exchange correlation energy.[31] The cutoff for the plane wave kinetic energy is set to 600 eV. The Monkhorst−Pack method is used to determine **k**-points grid for the Brillouin zone integration, which is 3 × 3 × 1 in the present supercell calculations. The atomic positions and lattice parameters were fully optimized, where the convergence criteria for the Hellmann−Feynman force for each atom was set to be 0.01 eV/Å. The electrochemical properties and the oxygen vacancy formation of NCM111 were calculated by a 2 × 2 × 2 supercell. For calculating the oxygen vacancy in the NCM111, one oxygen atom is extracted from the supercell. The minimum distance between two oxygen vacancies is 9.97Å, and the concentration for the oxygen vacancy in the material is 0.69%. All calculations were performed under a spin-polarization scheme, including ferromagnetic and antiferromagnetic configurations.

In order to describe the strong electron correlation interactions in the *d*-orbitals of the transition metal elements, the GGA+*U* method is adopted. Because different sets of *U* values had been reported for Ni, Co, and Mn elements in the literature,[32−36] we examined in detail the effects of three different sets of effective *U* values (i.e., $U_{eff} = U - J$; hereafter $J = 0$) on the electrochemical properties of $Li_xNi_{1/3}Co_{1/3}Mn_{1/3}O_2$ (x = 1, 2/3, 1/3, 0) (hereafter denoted Li_xNCM111). The *U* values employed in our calculations were U_1 = 6.0 3.4 3.9[34] (for Ni, Co, and Mn, respectively), U_2 = 6.0 5.5 4.2,[36] and U_3 = 5.0 5.0 5.0.[35] Wang et al. also reported first-principles estimations of the *U* parameters for several transition metals.[33] They reported *U* values to be 6.4 eV for Ni; 3.3 eV for Co; and 3.5, 3.8, or 4.0 eV for Mn. Because this set of *U* values was very close to U_1 = 6.0 3.4 3.9, only the U_1 was then calculated. The van der Waals interactions are not included in the calculations because the bonding in this material of NCM111 is mainly ionic mixed with covalent although it is a layered material.

3. RESULTS AND DISCUSSION

3.1. Structural Evolution and Voltage Profiles during Li-Ion Extractions. The structure of the perfect NCM111 calculated in this paper is based on the one with a space group of $P3_112$ shown in Figure 1a, which comes from Ohzuku.[37] This structure has also been employed in other theoretical

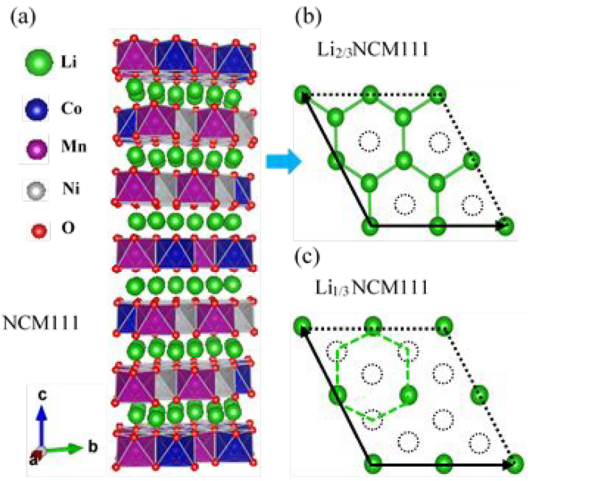

Figure 1. (a) Crystal structure of NCM111. (b and c) Schematic presentations of the top views of the lithium layers at (b) $Li_{2/3}$NCM111 (x = 2/3) and (c) $Li_{1/3}$NCM111 (x = 1/3). The dotted circles represent the extracted lithium ions.

calculations.[38] For the crystal structures of delithiated phases, we adopt here an approximate scheme to obtain the structures of $Li_xNi_{1/3}Co_{1/3}Mn_{1/3}O_2$ (x = 1, 2/3, 1/3, 0) in the process of Li extraction. For x = 1, the material is simply NCM111. For x = 2/3 where one-third of the lithium ions are deintercalated in NCM111 (i.e., for $Li_{2/3}$NCM111), the corresponding crystal structure of the Li-layer is shown in Figure 1b, which is the same for all the Li layers. The dotted circles represent the extracted lithium ions. When two-thirds of the lithium ions are extracted in NCM111 (i.e., x = 1/3 and for $Li_{1/3}$NCM111), more lithium ions at the three vertices of the hexagons in Figure 1b are removed, as shown in Figure 1c. In all these cases, Li ions are extracted uniformly. For x = 0, all the lithium ions are deintercalated from NCM111. Then, all the lithium layers disappear.

We first calculate the cohesive energies of NCM111 by using GGA (U = 0), GGA+U_1, GGA+U_2, and GGA+U_3 methods (with U_1 = 6.0 3.4 3.9 for Ni, Co, Mn, respectively, U_2 = 6.0 5.5 4.2, U_3 = 5.0 5.0 5.0), as well as under the spin-polarized scheme for both the ferromagnetic (FM) and antiferromagnetic (AFM) configurations. In this paper, we calculated the cohesive energies of NCM111 in three kinds of antiferromagnetic configurations. Case 1: all the spins of adjacent transition metal ions are in opposite directions (where the magnetic moments of Co are 0 μ_B). The cohesive energy (taken always to be positive) of such an AFM magnetic ordering is smaller (around 0.02 eV/supercell for all the *U* employed) than that of FM ordering. This means that FM should be favored by the system under such a magnetic ordering. Case 2: the spins in the Ni sublattice are in opposite directions to the Mn sublattice (again, magnetic moments of Co are 0 μ_B), while the spins in all the transition metal layers are parallel. Such a magnetic ordering had been described as AFM by Ceder et al.[18] (it should be noted that the antiferromagnetism mentioned here is actually ferrimagnetism, because the atomic magnetic moments of Ni, Co, Mn ions are all different). The calculations show that the cohesive energy of this AFM is larger than that of FM by about 0.30 eV/supercell

https://doi.org/10.1021/acsomega.2c00375
ACS Omega 2022, 7, 14875−14886

for all the U employed, implying that the system should favor this AFM, as compared with FM. Case 3: based on the AFM ordering in case 2, however, spins of transition metal ions are in different directions in the adjacent layers of the transition metals. The calculated cohesive energy is almost indistinguishable with that of AFM ordering in case 2. This is because there is one layer of lithium ions existing in between the transition metal layers, leading to a very weak superexchange interaction between the transition metal layers. The results show that the cohesive energy of this AFM is larger than that of FM (between 0.36 and 0.41 eV/supercell; see Table 1 below).

Table 1. Calculated Lattice Parameters and Cohesive Energy Differences ΔE_i between FM and AFM Configurations (72 f.u./supercell), by Using the GGA and GGA+U Methods*

	lattice parameters (Å)				
NCM111	FM-GGA+U_i		AFM-GGA+U_i		cohesive energy differences (eV)
U	$a = b$	c	$a = b$	c	ΔE_i
U = 0	2.88	14.30	2.88	14.30	−0.38
U_1 = 6.0 3.4 3.9	2.88	14.30	2.88	14.34	−0.37
U_2 = 6.0 5.5 4.2	2.88	14.37	2.88	14.35	−0.36
U_3 = 5.0 5.0 5.0	2.89	14.37	2.89	14.36	−0.41

*Lattice parameters of NCM111 (exptl[37,39]): $a = b$ = 2.867 Å, c = 14.246 Å

Table 1 presents the calculated lattice parameters and the cohesive energy differences between FM and AFM configurations for NCM111 (72 f.u. per supercell). As shown in Table 1, the computational lattice parameters of NCM111 agree rather well with experimental values. Because it is meaningless to compare directly the cohesive energies with different values of U, because of different Hamiltonian employed, only the cohesive energy difference $\Delta E_i = E(\text{FM-GGA+}U_i) - E(\text{AFM-GGA+}U_i)$ are presented.

We notice that the working temperature of the battery is usually much higher than the Curie temperature T_c; therefore, the electrochemical properties of NCM111 are insensitive to the magnetic ordering of the material. Furthermore, the cohesive energies of different magnetic orderings are rather close. In the discussions below, all the results are then based on the antiferromagnetic ordering of case 3 (unless otherwise indicated), which has the largest cohesive energy.

We now calculate the formation energies of $Li_xNCM111$ in each delithiated concentration (x = 1, 2/3, 1/3, 0) by the GGA +U method under different U values. The formation energy formula employed is as follows:[40]

$$E_f(x) = E(Li_xNCM111) - [xE(NCM111) + (1 - x)E(Ni_{1/3}Co_{1/3}Mn_{1/3}O_2)] \quad (1)$$

that is, the formation energy is calculated relative to the fully lithiated NCM111 and fully delithiated $Ni_{1/3}Co_{1/3}Mn_{1/3}O_2$ phases. Figure 2a demonstrates the convex hull plots for the calculated formation energies of $Li_xNCM111$ by using the GGA (U = 0) and GGA+U methods, as a function of Li concentration x. Results for different effective U values, i.e., (U_1 = 6.0 3.4 3.9, U_2 = 6.0 5.5 4.2, U_3 = 5.0 5.0 5.0), are presented. For GGA (U = 0) and GGA+U_1 calculations, two stable intermediate phases (i.e., $Li_{2/3}NCM111$ and $Li_{1/3}NCM111$) can be observed in the charging process. However, for GGA+U_2 and GGA+U_3 calculations, only one intermediate phase (i.e., $Li_{1/3}NCM111$) can be observed in the charging process. Also in Figure 2a, the formation energies for the GGA+U_1 and GGA+U_3 schemes are very close at Li concentration x = 2/3. In addition, the formation energies for the GGA+U_1 and GGA+U_2 methods are very close at Li concentration x = 1/3. The formation energies by the GGA method are always the largest (the absolute value) during the delithiation.

We then calculate the averaged voltages of $Li_xNCM111$ in the charging process. The averaged voltage formula employed is as follows:[18]

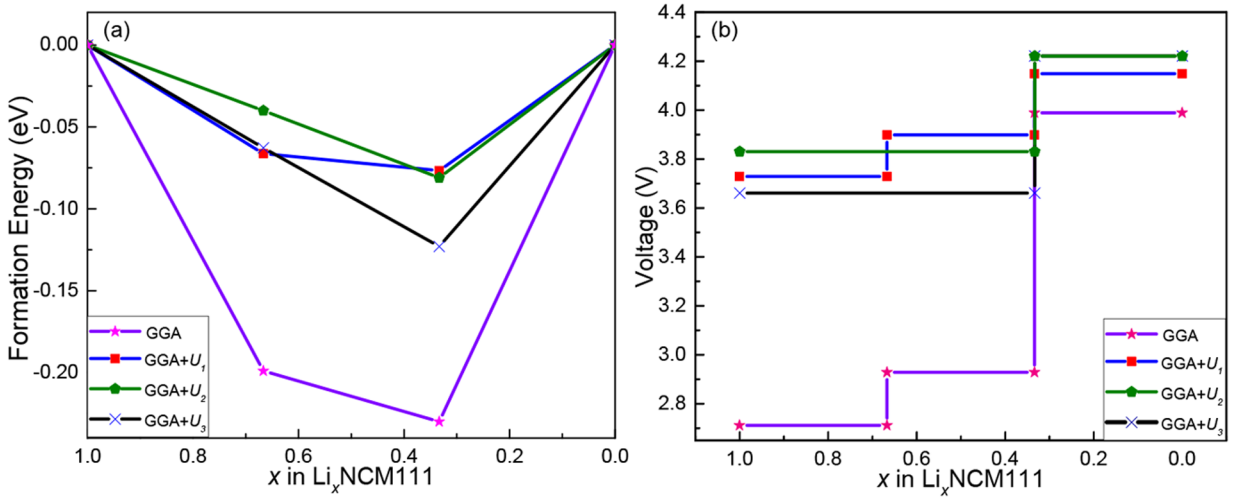

Figure 2. (a) The convex hull plots for the calculated formation energies and (b) the calculated averaged voltage curves of $Li_xNCM111$, as a function of Li concentration x, by using the GGA (U = 0) and GGA+U methods with different effective U values (i.e., U_1 = 6.0 3.4 3.9, U_2 = 6.0 5.5 4.2, and U_3 = 5.0 5.0 5.0).

https://doi.org/10.1021/acsomega.2c00375
ACS Omega 2022, 7, 14875−14886

$$V = -\frac{E(\mathrm{Li}_{x_2}\mathrm{NCM111}) - E(\mathrm{Li}_{x_1}\mathrm{NCM111}) - (x_2 - x_1)E(\mathrm{Li})}{(x_2 - x_1)} \quad (2)$$

where $E(\mathrm{Li}_{x_1}\mathrm{NCM111})$ and $E(\mathrm{Li}_{x_2}\mathrm{NCM111})$ are the cohesive energies of the material at Li concentrations of x_1 and x_2, respectively. E [Li] is the cohesive energy of a single Li atom in bulk lithium. As shown in Figure 2b, the first voltage plateau by using GGA ($U = 0$) method is around 2.74 V, while the second voltage plateau is 2.95 V. Such voltage plateaus are in basic agreement with those (e.g., 2.99 and 3.30 V) shown by Ohzuku et al.[37] The third average voltage plateau is about 3.99 V. The calculated first voltage platform by the GGA scheme is generally lower than the experimental value.[41] Generally speaking, the calculated voltage platforms by the GGA+U_i (i = 1, 2, 3) methods are all significantly higher than those of the GGA method. For the GGA+U_1 method, the three voltage plateaus are visibly different. However, for GGA+U_2 and GGA +U_3 calculations, there are only two voltage platforms that are very different. The maximum averaged voltage is achieved by the GGA+U_2 and GGA+U_3 scheme, which is about 4.24 V. Under the GGA+U_i (i = 1, 2, 3) methods, the calculated first voltage platform is between 3.65 and 3.83 V, which agrees well with the experimental value of 3.8 V.[41] In other words, the GGA ($U = 0$) scheme underestimates the first voltage plateau significantly, while GGA+U methods predict reasonably good values of the first voltage platform, as compared with the experimental value.

3.2. Electronic Structures and Redox Reactions during Li-Ion Extractions. The valence states of the isolated TM atoms in the NCM111, together with their electronic configurations and the magnetic moments, are shown in Table 2. The schematic plots of the 3d-orbital electron arrangements in the octahedral TM and oxygen ions (TM-O_6) ligand field in NCM111 are also presented in the table. Considering Table 2, it would be helpful to understand the electrochemical properties (e.g., redox reactions) during the delithiation process of NCM111.

Table 2. Electronic Configurations and the Magnetic Moments of the Isolated Transition Metal Atoms, the 3d-Orbital Electron Arrangements in the Octahedral TM-O_6 Ligand Field, and the Corresponding Atomic Valence States in NCM111.

	Electron configuration (isolated atoms)	Number of atoms (in supercell)	Atomic magnetic moment /μ_B	3d-orbital electron arrangement	Valence state (in NCM111)
Ni	$3d^8 4s^2$	24	2	e_g ↿ ↿ / t_{2g} ↿⇂ ↿⇂ ↿⇂	Ni^{2+}
Co	$3d^7 4s^2$	24	0	e_g — — / t_{2g} ↿⇂ ↿⇂ ↿⇂	Co^{3+}
Mn	$3d^5 4s^2$	24	3	e_g — — / t_{2g} ↿ ↿ ↿	Mn^{4+}

First, the magnetic moments of the $Li_xNCM111$ (x = 1, 2/3, 1/3, 0) during the delithiation are calculated by the GGA (U = 0) method, and the results are presented in Table 3. It is helpful to perform GGA calculations, in order to compare the GGA+U_i calculations with different values of U_i. Here, the changes in the magnetic moments are analyzed to help characterize the charge compensation mechanisms during the delithiation (for $U = 0$). For $1 \geq x \geq 2/3$, where in total 24 Li ions are extracted from the supercell, the results show that there are correspondingly 24 Ni^{2+} ions oxidized, changing their magnetic moments from 2 μ_B to 1 μ_B and their valence from Ni^{2+} to Ni^{3+}. Actually, 12 of the 24 Ni^{2+} ions lose one spin-up electron in the e_g band (see Table 2), and the other 12 Ni^{2+} ions lose one spin-down electrons in the e_g band, leading to magnetic moment change from 2 μ_B to 1 μ_B. For $2/3 \geq x \geq 1/3$, when 24 Li ions are further extracted, again, there are 24 Ni^{3+} ions oxidized, changing their magnetic moments from 1 μ_B to 0 μ_B and their valence states from Ni^{3+} to Ni^{4+} ions. When the NCM111 are fully delithiated (i.e., $1/3 \geq x \geq 0$), that is, the remaining 24 Li ions are deintercalated, the results suggest that 24 Co^{3+} ions are now oxidized, transforming their magnetic moments from 0 μ_B to 1 μ_B and their valences from Co^{3+} to Co^{4+} (see Table 2, where one electron is lost in the t_{2g} band for each Co^{3+}). In this region, i.e., $1/3 \geq x \geq 0$, Ni ions do not participate in the redox reaction because all the Ni ions are now Ni^{4+}. During the whole delithiation process, all 24 Mn ions are not involved in the redox reactions, keeping Mn^{4+} and magnetic moment of 3 μ_B unchanged. Summarizing, for $1 \geq x \geq 2/3$ and $2/3 \geq x \geq 1/3$, it is the Ni ions who are in charge of the compensation of electrons, while for $1/3 \geq x \geq 0$, it is the Co ions who participate in the redox reaction. These results on the redox reactions are consistent with those of Cedar et al. at every delithiated concentration and the experimental results as well.[18,22,37,38,42]

Table 3. Magnetic Moments of $Li_xNCM111$ (x = 1, 2/3, 1/3, 0) from GGA (U = 0) Calculations[a]

$Li_xNCM111$	magnetic moments (μ_B) GGA (U = 0) calculations		
x	Ni	Co	Mn
1	1.54 (12)	0 (24)	2.73 (12)
	−1.54 (12)		−2.73 (12)
2/3	0.75 (12)	0 (24)	2.73 (12)
	−0.75 (12)		−2.73 (12)
1/3	0 (24)	0.20 (12)	2.70 (12)
		−0.20 (12)	−2.70 (12)
0	0 (24)	0.58 (12)	2.61 (12)
		−0.58 (12)	−2.61 (12)

[a]The parentheses following the magnetic moment contain the number of atoms in the supercell.

The magnetic moments of the $Li_xNCM111$ (x = 1, 2/3, 1/3, 0) during the delithiation process are also calculated by using the GGA+U_i methods (with U_1 = 6.0 3.4 3.9, U_2 = 6.0 5.5 4.2, and U_3 = 5.0 5.0 5.0), and results are shown in Table 4. The changes of magnetic moments of TM ions during the delithiation by using the GGA+U_1 calculations are visibly different from those using the GGA+U_2 and GGA+U_3 calculations (it is worth noting that the changes of magnetic moments of TM ions for GGA+U_2 and GGA+U_3 schemes are very close). In the following discussion, only the results from GGA+U_1 and GGA+U_2 calculations are to be compared.

https://doi.org/10.1021/acsomega.2c00375
ACS Omega 2022, 7, 14875−14886

Table 4. Magnetic Moments of $Li_xNCM111$ (x = 1, 2/3, 1/3, 0), Calculated by Using the GGA+U_i Method with Three Sets of different U_i .(i.e., U_1 = 6.0 3.4 3.9, U_2 = 6.0 5.5 4.2, U_3 = 5.0 5.0 5.0)[a]

$Li_xNCM111$	magnetic moments (μ_B)		
	GGA+U_1 (U_1 = 6.0 3.4 3.9)		
x	Ni	Co	Mn
1	1.74(12)	0 (24)	3.16(12)
	−1.74(12)		−3.16(12)
2/3	1.73(12)	1.09(12)	3.16(12)
	−1.73(12)	−1.09(12)	−3.16(12)
1/3	0.99(12)	1.12(12)	3.17(12)
	−0.99(12)	−1.12(12)	−3.17(12)
0	0.13(12)	1.02(12)	3.20(12)
	−0.13(12)	−1.02(12)	−3.20(12)
GGA+U_2 (U_2 = 6.0 5.5 4.2)			
x	Ni	Co	Mn
1	1.74 (12)	0 (24)	3.21 (12)
	−1.74 (12)		−3.21 (12)
2/3	1.02 (12)	0 (24)	3.19 (12)
	−1.02 (12)		−3.19 (12)
1/3	0 (24)	0 (24)	3.15(12)
			−3.15(12)
0	0 (24)	1.25 (12)	3.20(12)
		−1.25 (12)	−3.20(12)
GGA+$U3$ (U_3 = 5.0 5.0 5.0)			
x	Ni	Co	Mn
1	1.70 (12)	0 (24)	3.32 (12)
	−1.70 (12)		−3.32 (12)
2/3	0.97 (12)	0 (24)	3.31 (12)
	−0.97 (12)		−3.31 (12)
1/3	0 (24)	0 (24)	3.31 (12)
			−3.31 (12)
0	0 (24)	1.15 (12)	3.31 (12)
		−1.15 (12)	−3.31 (12)

[a]The parentheses following the magnetic moment contain the number of atoms in the supercell.

For $1 \geq x \geq 2/3$, where 24 Li ions are extracted from the supercell, the results of GGA+U_1 in Table 4 show that there are correspondingly 24 Co^{3+} ions now oxidized, transforming their magnetic moments from 0 μ_B to 1 μ_B and Co^{3+} ions to Co^{4+} ones (where one electron is lost in the t_{2g} band for each Co^{3+}, see Table 2). In this case, Ni and Mn ions are not involved in the redox reactions. For $1 \geq x \geq 2/3$ and for GGA +U_2 calculations, Table 4 suggests that 24 Ni^{2+} ions are now oxidized, changing from Ni^{2+} to Ni^{3+} and their magnetic moments from 2 μ_B to 1 μ_B. Actually, 12 of the 24 Ni^{2+} ions lose one spin-up electron in the e_g band (see Table 2); the other 12 Ni^{2+} ions lose one spin-down electron in the e_g band. Clearly, the charge compensation mechanisms during delithiation for $1 \geq x \geq 2/3$ are completely different for GGA+U_1 and GGA+U_2 results. For $2/3 \geq x \geq 1/3$, when 24 Li ions are further extracted from the supercell, the results for GGA+U_1 shown in Table 4 suggest that there are 24 Ni^{2+} ions oxidized, changing their magnetic moments from 2 μ_B to 1 μ_B and Ni^{2+} to Ni^{3+}. However, for $2/3 \geq x \geq 1/3$ and for GGA +U_2 calculations, Table 4 indicates that 24 Ni^{3+} ions are oxidized, changing from Ni^{3+} to Ni^{4+} ions and their magnetic moments from 1 μ_B to 0 μ_B. In this case, again, the charge compensation mechanisms during delithiation for $2/3 \geq x \geq 1/3$ are different for GGA+U_1 (where Ni^{2+} oxidized to Ni^{3+}) and GGA+U_2 (where Ni^{3+} oxidized to Ni^{4+}) calculations.

When NCM111 are fully delithiated (i.e., $1/3 \geq x \geq 0$), that is, the remaining 24 Li ions in the supercell are fully deintercalated, for the GGA+U_1 calculations, there are 24 Ni^{3+} ions oxidized, changing from Ni^{3+} to Ni^{4+} ions and their magnetic moments from 1 μ_B to 0 μ_B. However, for GGA+U_2 calculations, the results in Table 4 suggest that 24 Co^{3+} ions are oxidized, transforming from Co^{3+} to Co^{4+} and their magnetic moments from 0 μ_B to 1 μ_B (see Table 2, where one electron is lost in the t_{2g} band for each Co^{3+}). Again, the charge compensation mechanisms are different for GGA+U_1 and GGA+U_2 calculations. During the whole delithiation process, all 24 Mn-ions in the supercell are not involved in the redox reactions. The charge compensation mechanism from GGA +U_2 and GGA+U_3 calculations is in agreements with the experimental results; however, the GGA+U_1 calculations are not.

As we discussed previously, different sets of U values (reminding that they all come from careful studies in the literatures) can lead to different charge compensation mechanisms in the delithiation process. In the following discussions, the spin-polarized partial density of states (PDOS) of TM ions are analyzed to further understand the charge compensation mechanisms during the delithiation, under different values of U employed.

We first discuss the results of PDOS calculated by using the GGA method (with U = 0). When 24 Li ions are extracted from the supercell (i.e., $1 \geq x \geq 2/3$), it is clear that only the green peaks of Ni-3d electrons on the PDOS plot cross the Fermi level, indicating the valence electron loss of Ni-3d orbitals (see Figure 3a,b). That is, the Ni^{2+} ions are oxidized into Ni^{3+} ones, and the redox reaction is Ni^{2+}/Ni^{3+}. For $2/3 \geq x \geq 1/3$, where another 24 Li^+ ions are further extracted, we can see that more green peaks of Ni-3d electrons on the PDOS plot cross the Fermi level (see Figure 3b,c), then the redox reaction of Ni^{3+}/Ni^{4+} takes place in this range of $2/3 \geq x \geq 1/3$. When NCM111 are fully delithiated (i.e., $1/3 \geq x \geq 0$ and the remaining 24 Li^+ ions are all deintercalated), we find that only the blue peaks of Co-3d electrons on PDOS plot cross the Fermi level (as shown in Figure 3c,d), suggesting that Co ions are now participating in the redox process, with Co^{3+} ions oxidized to Co^{4+} ones. During the whole delithiation process, the purple peaks of Mn-3d electrons do not cross the Fermi level, keeping Mn^{4+} valence unchanged. That is, Mn^{4+} ions are not involved in the redox reactions. All the charge compensation mechanisms of TM ions discussed based on the PDOS here are consistent with the analysis of the changes of the magnetic moments of TM ions during delithiation.

We now compare the charge compensation mechanisms of TM ions from the calculated PDOS's by using GGA+U_1 and GGA+U_2 methods. Figures 4 and 5 present the calculated PDOS's of the Ni-3d, Co-3d, Mn-3d, and O-2p from both the GGA+U_1 (U_1 = 6.0 3.4 3.9) and GGA+U_2 (U_2 = 6.0 5.5 4.2) calculations, respectively, for $Li_xNCM111$ (x = 1, 2/3, 1/3, 0) during the delithiation process. For $1 \geq x \geq 2/3$ and for GGA +U_1 calculations, where 24 Li^+ ions are extracted from the supercell, we can clearly see from Figure 4a,b that only the blue peaks of Co-3d electrons cross the Fermi level, which indicates that redox reaction of Co^{3+}/Co^{4+} takes place. For the same range of $1 \geq x \geq 2/3$ but for GGA+U_2 calculations, however, Figure 5a,b shows that only the green peaks of Ni-3d electrons cross the Fermi level, suggesting that Ni ions participate in the

https://doi.org/10.1021/acsomega.2c00375
ACS Omega 2022, 7, 14875−14886

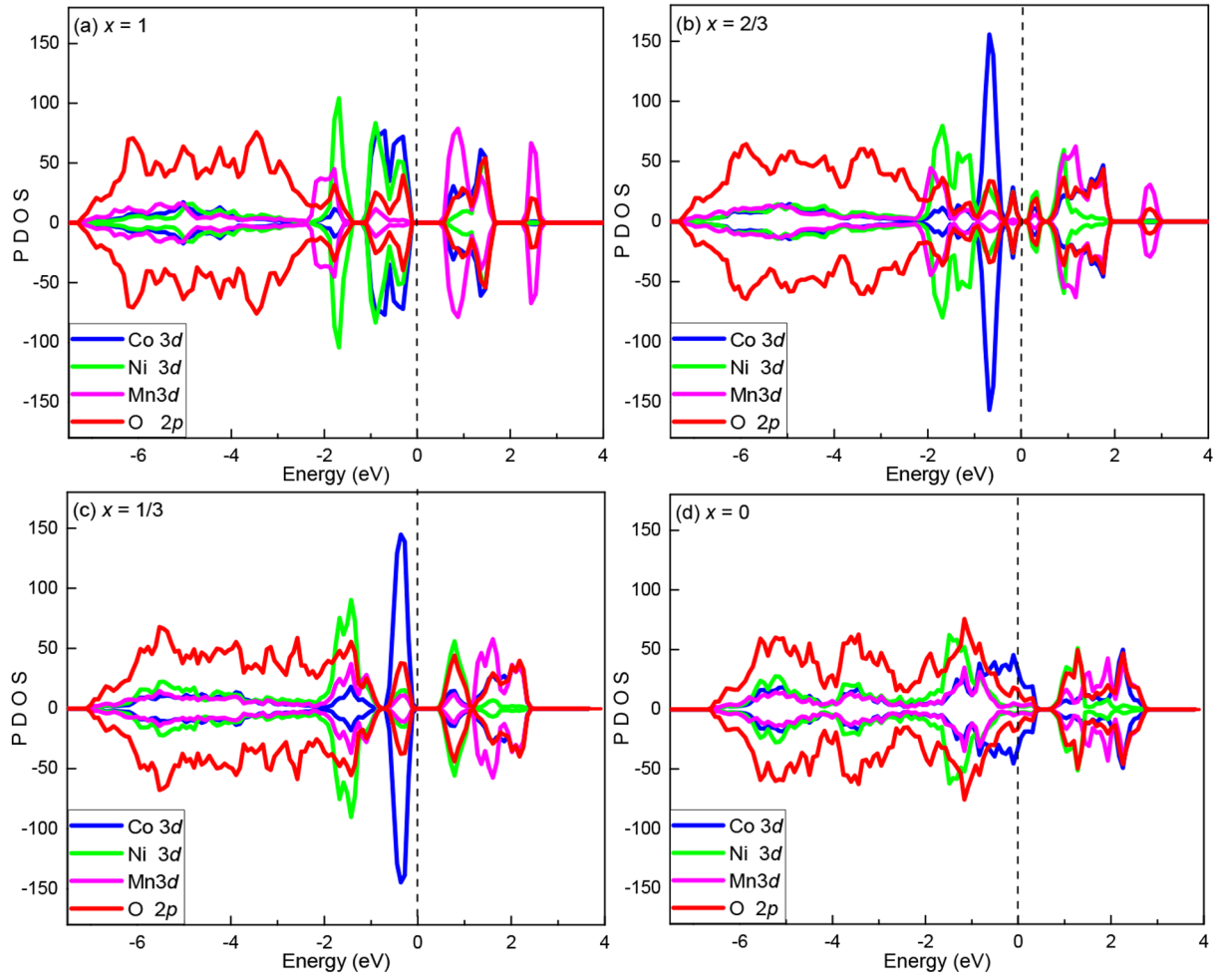

Figure 3. Partial density of states calculated by the GGA method with $U = 0$, for (a) $x = 1$, (b) $x = 2/3$, (c) $x = 1/3$, and (d) $x = 0$. Fermi levels are represented by dashed vertical lines.

redox reaction and Ni^{2+} ions are oxidized to Ni^{3+}. For $2/3 \geq x \geq 1/3$ and for GGA+U_1 calculations, where 24 Li^+ ions are further extracted from the supercell, only the green peaks of Ni-3*d* electrons are found to cross the Fermi level (see Figure 4b,c), indicating that redox reaction of Ni^{2+}/Ni^{3+} takes place in this range of $2/3 \geq x \geq 1/3$. For GGA+U_2 calculations and for the same range of $2/3 \geq x \geq 1/3$, from Figure 5b,c, the green peaks of Ni-3*d* electrons cross the Fermi level, suggesting that Ni ions take part in the redox reaction and Ni^{3+} ions are oxidized to Ni^{4+}. Finally, for $1/3 \geq x \geq 0$, when the remaining 24 Li^+ ions are fully deintercalated, it is shown that green peaks of Ni-3*d* electrons cross the Fermi level for the GGA+U_1 calculations (see Figure 4c,d), while it is the blue peaks of Co-3*d* electrons that cross the Fermi level for the GGA+U_2 calculations (see Figure 5c,d). Here, Ni^{3+} ions are oxidized to Ni^{4+} ones from the GGA+U_1 method, while it is the Co^{3+} ions who are oxidized to Co^{4+} ones from the GGA+U_2 method. The Mn^{4+} ions are not involved in the redox reaction during the whole delithiation process because no peaks of Mn-3*d* electrons cross the Fermi level. Again, analysis based on PDOS is consistent with the analysis based on the changes of the magnetic moments.

In summary, the charge compensation mechanisms are completely different for GGA+U_1 and GGA+U_2 calculations during the whole delithiation process. The Co^{3+}/Co^{4+}couples were shown to dominate the redox reaction for $1 \geq x \geq 2/3$ from the GGA+U_1 (U_1 = 6.0 3.4 3.9) method; however, it is the Ni^{2+}/Ni^{3+}couples who dominate the redox reaction for the same range of $1 \geq x \geq 2/3$ from the GGA+U_2 (U_2 = 6.0 5.5 4.2) method. Furthermore, Ni^{2+}/Ni^{3+} and Ni^{3+}/Ni^{4+} couples dominated the redox reactions for $2/3 \geq x \geq 1/3$ and $1/3 \geq x \geq 0$, respectively, for the GGA+U_1 calculations; however, it is the Ni^{3+}/Ni^{4+} and Co^{3+}/Co^{4+} couples who dominated the redox reactions in the same regions of concentrations for the GGA+U_2 calculations. Considering that all the *U* values of TM metals come from careful studies in the literature (the theoretical calculations are declared as *ab initio*), it seems that the experimental charge compensation processes during delithiation are still of great importance to evaluate the theoretical calculations.

Although cationic redox reactions are shown to dominate the electrochemical processes in NCM111 electrode material,[18,22,37,38,42] it has also been shown that both cationic and anionic redox reactions exist in the NCM111. Reversible intrinsic lattice oxygen redox reactions at high potentials were clearly revealed.[43] Therefore, the understanding of O activities are important for utilizing the full potential of these cathode materials.

The calculated PDOS's of O-2*p* states by the GGA, GGA+U_1, and GGA+U_2 methods in Li_xNCM111 for $x = 0.2$ and $x = 0.125$ are compared in Figure 6. It can be seen that PDOS plots for $x = 0.2$ and $x = 0.125$ are rather close. It is also clear

https://doi.org/10.1021/acsomega.2c00375
ACS Omega 2022, 7, 14875−14886

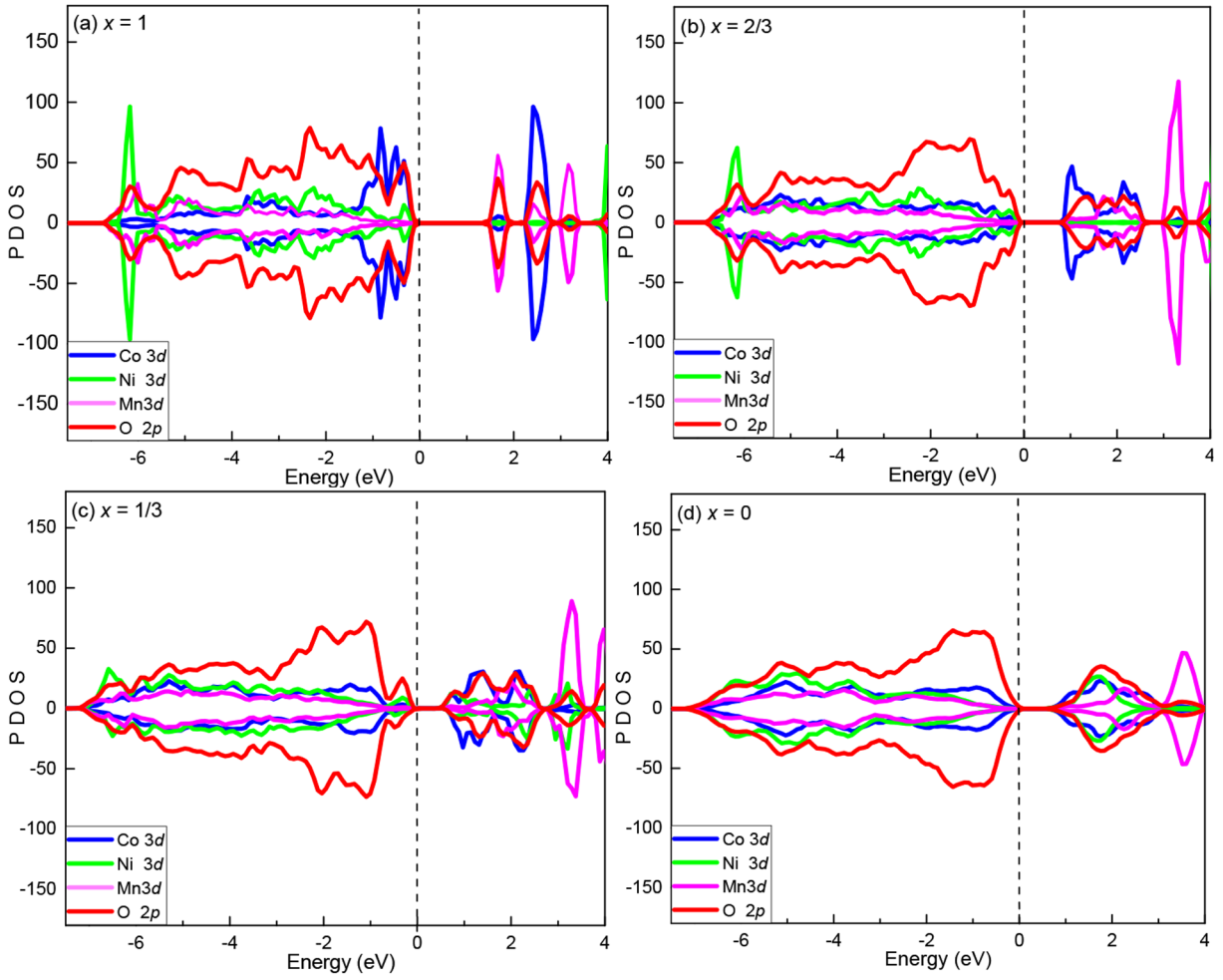

Figure 4. Partial density of states calculated by the GGA+U_1 method with U_1 = (6.0 3.4 3.9), for (a) x = 1, (b) x = 2/3, (c) x = 1/3, and (d) x = 0. Fermi levels are represented by dashed vertical lines.

that the PDOS plots of O-2p electrons for both the GGA+U_1 and GGA+U_2 schemes are quite alike. However, the calculated PDOS's of O-2p electrons by the GGA (U = 0) method are quite different from those by the GGA+U_1 and GGA+U_2 methods. For lower levels of delithiation (i.e., relatively low potentials) in Li$_x$NCM111, our calculations indicate that O anions do not participate in the redox process, which is in agreement with the previous theoretical and experimental studies.[18,38,42] For deep delithiation levels (i.e., high potentials), Figure 6 demonstrates that O anions are visibly involved in the redox reactions (for x = 0.2 and x = 0.125), which is also consistent with the previous experimental and theoretical results.[27,43]

The involvement of oxygen in the redox process in NCM111 can be understood through the analysis of the interactions of oxygen with their neighboring ions. Oxygen atoms in NCM111 are coordinated with both the Li^+ and TM ions. Therefore, the interactions of O with the coordinated atoms come from two aspects: one is the attractive electrostatic interactions between Li and O ions, and the other is the hybridization of the TM-O orbitals which is mainly covalent in nature. The delithiation process weakens the attractive electrostatic interaction between Li-O ions and strengthens the TM-O hybridizations. When the number of the removed lithium ions is small (lower potential), although some of the O-2p energy levels are pushed toward the Fermi level, the O-2p orbitals do not cross to the Fermi surface. This indicates that O ions are not involved in the redox reaction at low potentials. However, at high potentials (see Figure 6), the attractive electrostatic interaction between the Li-O ions are much weakened and the TM-O hybridizations are further strengthened. Such combined ionic and covalent interactions of O with the neighboring ions result in some of the energy levels of oxygen being pushed to cross the Fermi surface, suggesting that oxygen ions are capable of participating in the anionic redox processes in NCM111 at high potentials.

3.3. Formation Energy of an Oxygen Vacancy in NCM111 Material. The release of oxygen in the NCM111 cathode is directly related to the formation energy of oxygen vacancy in this material. Here, we study the variation of the oxygen vacancy formation energy in NCM111 versus the temperature and oxygen partial pressure in order to understand the stability of the lattice oxygen. The oxygen vacancy is calculated by extracting one oxygen atom from the supercell of NCM111. The formation energy of oxygen vacancy in charge state q, $E_f(O^q)$, can be defined according to the following equation:[44]

$$E_f(O^q) = E(O^q) - E(0) + \Delta n\mu_O + q(E_{VBM} + \varepsilon_F) \quad (3)$$

where $E(O^q)$ is the cohesive energy of the supercell with an oxygen vacancy in charge state q, $E(0)$ is the cohesive energy

https://doi.org/10.1021/acsomega.2c00375
ACS Omega 2022, 7, 14875−14886

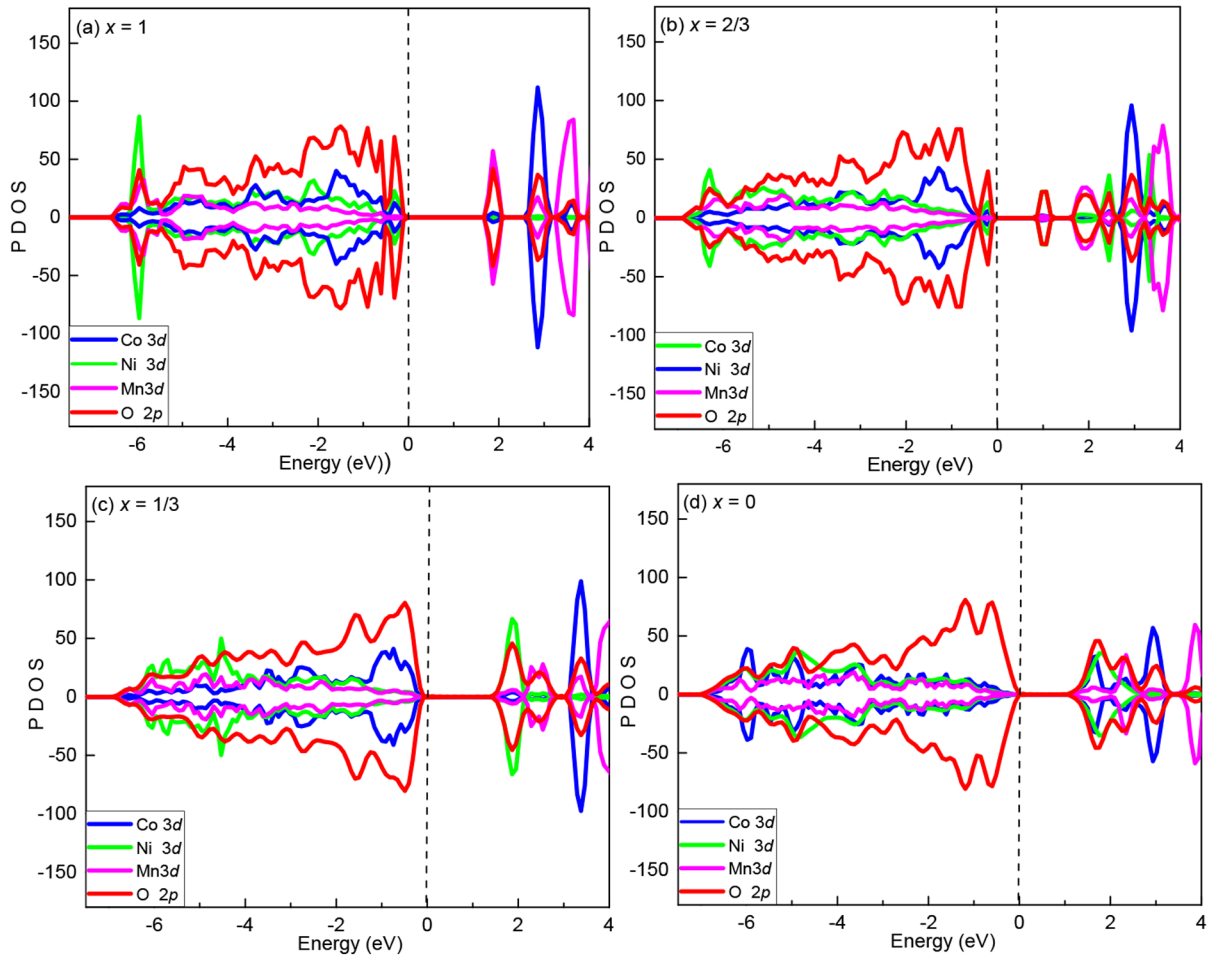

Figure 5. Partial density of states calculated by the GGA+U_2 method with U_2 = (6.0 5.5 4.2), for (a) x = 1, (b) x = 2/3, (c) x = 1/3, and (d) x = 0. Fermi levels are represented by dashed vertical lines.

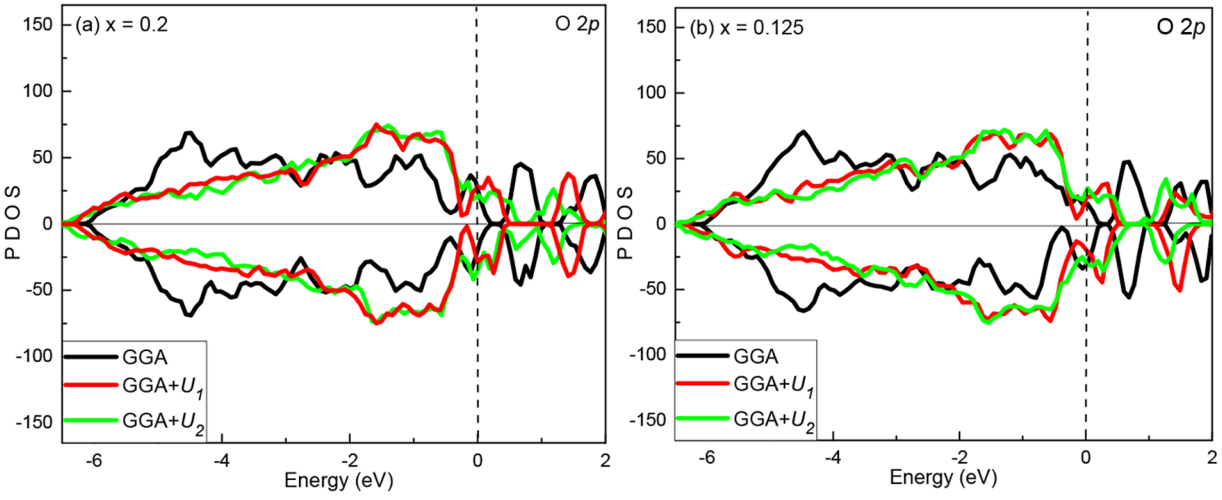

Figure 6. PDOS of O-2p states calculated by GGA, GGA+U_1, and GGA+U_2 methods with U_1 = 6.0 3.4 3.9 and U_2 = 6.0 5.5 4.2 for (a) x = 0.2 and (b) x = 0.125 in $Li_xNCM111$. Fermi levels are represented by dashed lines.

of the perfect supercell in the bulk phase of NCM111 (without vacancy), and Δn represents the number of oxygen atoms which have been removed from the perfect supercell in forming the oxygen vacancies. ε_F is the Fermi level. In this paper, only the neutral oxygen vacancy is calculated; therefore, q = 0 and the formation energy of an oxygen vacancy is independent of the charge state of the O vacancy and the Fermi level of the system.

In eq 3, μ_O is the chemical potential of O atom, representing the energy of the reservoir with which the extracted O atoms

https://doi.org/10.1021/acsomega.2c00375
ACS Omega 2022, 7, 14875−14886

are exchanged. We calculate the oxygen chemical potential μ_O by the following formula:[45]

$$\mu_O(P, T) = \mu_O(P_0, T_0) + \mu_O(P_1, T) + \frac{1}{2}k_B T \ln\left(\frac{P}{P_1}\right) \quad (4)$$

where $\mu_O(P_0, T_0)$ represents the oxygen chemical potential at zero pressure ($P_0 = 0$) and zero temperature ($T_0 = 0$), which is approximated to half of the total cohesive energy of an isolated O_2 molecule obtained by the DFT calculations $\left(\frac{1}{2}E(O_2)\right)$. The second term in eq 4, $\mu_O(P_1, T)$, originated from experimental data,[46] expressing the contribution of the temperature to the oxygen chemical potential at a particular pressure P_1 (here, P_1 = 1 atm). The third term in eq 4 represents the contribution of pressure to the chemical potential of oxygen μ_O (P, T), when the gas-phase oxygen is treated as an ideal gas. k_B is the Boltzmann's constant.

There are three kinds of nonequivalent oxygen vacancies (represented by O_1, O_2, and O_3) in NCM111. The formation energy of an oxygen vacancy in NCM111 is calculated by using GGA+U_i methods with three sets of U_i (i.e., U_1 = 6.0 3.4 3.9, U_2 = 6.0 5.5 4.2, and U_3 = 5.0 5.0 5.0) as well as for three nonequivalent oxygen vacancies. The O-vacancy formation energies under zero temperature and zero pressure are given in Table 5. Table 5 suggests that the oxygen vacancy formation energies for different U values and for nonequivalent oxygen vacancies (O_1, O_2, and O_3) in NCM111 are all relatively close. Therefore, in the following discussions, the results only from GGA+U_1 with U_1 = (6.0 3.4 3.9) will be presented and analyzed.

Table 5. Oxygen Vacancy Formation Energies at Zero Temperature and Zero Pressure in Bulk NCM111, for Three Nonequivalent Oxygen Vacancies under Three Sets of Different Values of *U*

	O-vacancy formation energies (eV)		
NCM111	U_1 = 6.0 3.4 3.9	U_2 = 6.0 5.5 4.2	U_3 = 5.0 5.0 5.0
O_1	3.43	3.13	3.06
O_2	3.50	3.22	3.16
O_3	3.38	3.08	3.02

According to eqs 3 and 4, the formation energy of an oxygen vacancy is a function of the oxygen chemical potential which is dependent on the experimental conditions, such as the temperature and pressure. We now discuss the relationship of the O vacancy formation energy versus the temperature and the oxygen partial pressure. Figure 7 presents the formation energies of an oxygen vacancy as a function of temperature for three different types of oxygen vacancies, at the given oxygen partial pressure P = 0.2 atm and P = 100 atm, respectively. Results in Figure 7 indicate that the O vacancy formation energy decreases with increasing temperature for both oxygen partial pressures P = 0.2 atm and P = 100 atm, as expected. Upon comparing panels a and b of Figure 7, the results also suggest that the formation energy of an oxygen vacancy decreases with temperature faster at lower oxygen partial pressure p. Figure 8 shows the formation energies of an oxygen vacancy as a function of oxygen partial pressures, at the given T = 300 K and T = 1500 K, again for the three different types of oxygen vacancies. The results indicate that the formation energy of the O vacancy increases with the increase of oxygen partial pressure, implying that higher pressure should inhibit the formation of O vacancies. Upon comparing panels a and b of Figure 8, it is found that the O vacancy formation energy increases with the oxygen partial pressure more substantially at higher temperatures.

Then, the effects of both the temperature and oxygen partial pressure on the formation energy of an O vacancy are investigated, and the results are shown in Figure 9. Generally speaking, the formation energy of O vacancy decreases with the increase of temperature and the decrease of oxygen partial pressure, which is consistent with the previous discussions. For example, at the highest temperature of 1500 K and the lowest pressure of 10^{-10} atm shown in Figure 8b, the formation energy of oxygen vacancy consequentially reaches the lowest value. From the gradient of color shown in Figure 9, we can also see that the formation energy of an O vacancy changes more severely with the temperature, while less obviously with the oxygen partial pressure. In summary, the calculations show that the decreased temperature and the increased oxygen

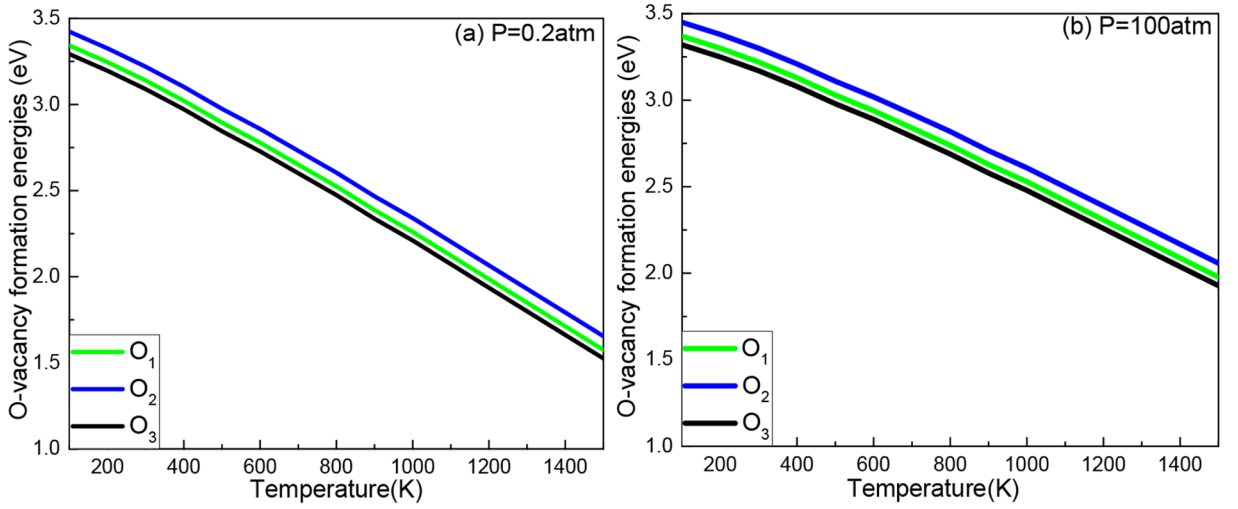

Figure 7. Formation energies of oxygen vacancy as a function of temperature for three nonequivalent oxygen vacancies, at oxygen partial pressure of (a) P = 0.2 atm and (b) P = 100 atm in the NCM111 material.

https://doi.org/10.1021/acsomega.2c00375
ACS Omega 2022, 7, 14875−14886

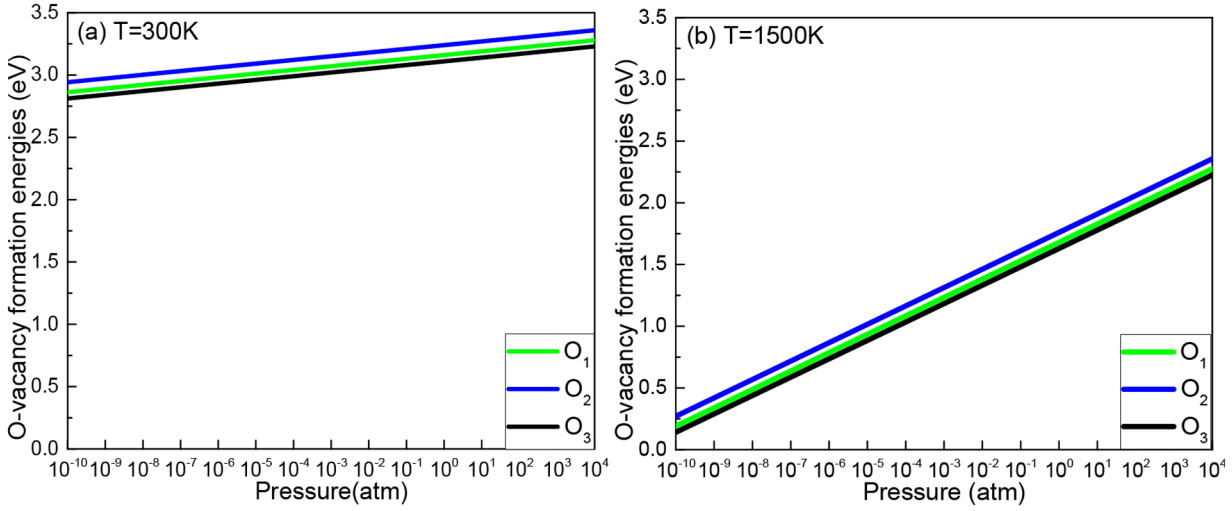

Figure 8. Formation energies of an oxygen vacancy as a function of oxygen partial pressure for three nonequivalent oxygen vacancies, at (a) T = 300 K and (b) T = 1500 K.

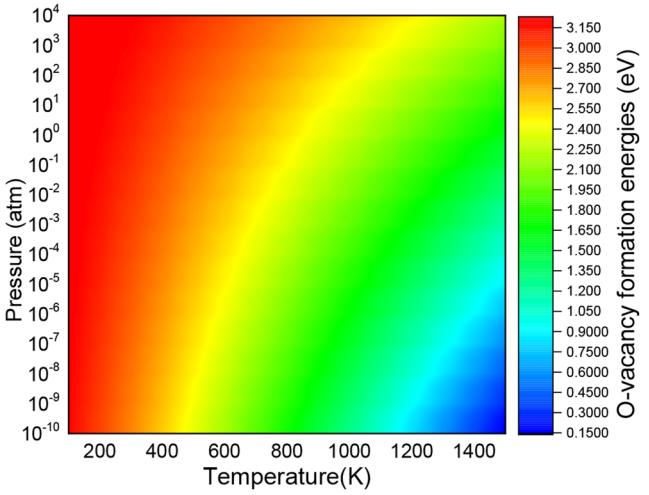

Figure 9. Formation energies of an oxygen vacancy (only for the third type of O_3 vacancy) as a function of both the temperature and oxygen partial pressure.

partial pressure can suppress the formation of the oxygen vacancy. Therefore, to govern the appearance of oxygen vacancies, one can decrease or increase the temperature and/or the pressure. These results are helpful for us to understand the factors that control the formation of oxygen vacancies and provide guidance for reducing the oxygen release and improving the stability of the lattice oxygen in the cathode materials of lithium-ion batteries.

4. CONCLUSIONS

In conclusion, we have employed first-principles calculations to study the electronic structures and electrochemical properties of $LiNi_{1/3}Co_{1/3}Mn_{1/3}O_2$ during the delithiation process. In particular, charge compensation mechanisms during the delithiation were compared carefully with the GGA and GGA+U methods under different U values reported in the literature. Comparisons between ferromagnetic and antiferromagnetic configurations were also conducted. The results suggested that the electrochemical properties (e.g., the redox reactions) were clearly dependent on the values of parameter U, i.e., different sets of U values could lead to different charge compensation mechanisms in the delithiation process. For example, Co^{3+}/Co^{4+} couples were shown to dominate the redox reaction for $1 \geq x \geq 2/3$ by using the GGA+U_1 method (U_1 = 6.0 3.4 3.9 for Ni, Co, and Mn, respectively). However, the Ni^{2+}/Ni^{3+} couple should be responsible for the redox reaction for $1 \geq x \geq 2/3$ by using the GGA+U_2 (U_2 = 6.0 5.5 4.2) method. According to our studies, experimental charge compensation processes during delithiation are then of great importance to evaluate the theoretical calculations (although theoretical calculations are declared as *ab initio*). The results also suggest that all the GGA+U_i methods predict better voltage platforms than the GGA method. The oxygen anionic redox reactions are also compared under different sets of U values. The electronic density of states and the magnetic moments of transition metals during the lithium extractions are employed to illustrate the redox reactions, under the GGA and GGA+U calculations with different values of U.

We have also investigated the formation energies of an oxygen vacancy in the bulk phase of NCM111 employing different U values, which is important for understanding the possible occurrence of the oxygen release. The increased temperature and/or decreased oxygen partial pressure decrease the formation energy of the O vacancy; that is, the lower temperature and higher oxygen partial pressure can suppress the formation of the oxygen vacancy. These calculations can help understand the formation of oxygen vacancies and provide guidelines for reducing the oxygen release and improving the stability of the lattice oxygen in this cathode material.

AUTHOR INFORMATION

Corresponding Author

Zizhong Zhu − *Department of Physics and Fujian Provincial Key Laboratory of Theoretical and Computational Chemistry, Xiamen University, Xiamen 361005, China;* orcid.org/0000-0003-3479-8148; Email: zzzhu@xmu.edu.cn

Authors

Xiao-Hong Shi − *Department of Physics, Xiamen University, Xiamen 361005, China*

https://doi.org/10.1021/acsomega.2c00375
ACS Omega 2022, 7, 14875−14886

Ya-Ping Wang − *Department of Physics, Xiamen University, Xiamen 361005, China*
Xinrui Cao − *Department of Physics and Fujian Provincial Key Laboratory of Theoretical and Computational Chemistry, Xiamen University, Xiamen 361005, China;* orcid.org/0000-0002-2998-8863
Shunqing Wu − *Department of Physics, Xiamen University, Xiamen 361005, China;* orcid.org/0000-0002-2545-0054
Zhufeng Hou − *State Key Laboratory of Structural Chemistry, Fujian Institute of Research on the Structure of Matter, Chinese Academy of Sciences, Fuzhou 350002, China;* orcid.org/0000-0002-0069-5573

Complete contact information is available at: https://pubs.acs.org/10.1021/acsomega.2c00375

Notes

The authors declare no competing financial interest.

■ ACKNOWLEDGMENTS

This work is supported by the National Key R&D Program of China under Grant No. 2016YFA0202601 and the National Natural Science Foundation of China under Grant No. 11874307.

■ REFERENCES

(1) Goodenough, J. B.; Kim, Y. Challenges for Rechargeable Li Batteries. *Chem. Mater.* **2010**, *22*, 587−603.
(2) Etacheri, V.; Marom, R.; Elazari, R.; Salitra, G.; Aurbach, D. Challenges in the Development of Advanced Li-ion Batteries: A Review. *Energy Environ. Sci.* **2011**, *4*, 3243−3262.
(3) Mizushima, K.; Jones, P. C.; Wiseman, P. J.; Goodenough, J. B. Li_xCoO_2 ($0< x < -1$): A New Cathode Material for Batteries of High Energy Density. *Mater. Res. Bull.* **1980**, *15*, 783−789.
(4) Wang, H.; Jang, Y. I.; Huang, B.; Sadoway, D. R.; Chiang, Y. M. TEM Study of Electrochemical Cycling-Induced Damage and Disorder in $LiCoO_2$ Cathodes for Rechargeable Lithium Batteries. *J. Electrochem. Soc.* **1999**, *146*, 473−480.
(5) Du Pasquier, A.; Plitz, I.; Menocal, S.; Amatucci, G. A Comparative Study of Li-ion Battery, supercapacitor and nonaqueous Asymmetric Hybrid Devices for Automotive Applications. *J. Power Sources* **2003**, *115*, 171−178.
(6) Reynier, Y.; Graetz, J.; SwanWood, T.; Rez, P.; Yazami, R.; Fultz, B. Entropy of Intercalation in Li_xCoO_2. *Phys. Rev. B.* **2004**, *70*, 174304.
(7) Wang, Z. G.; Wang, Z. X.; Peng, W. J.; Guo, H. J.; Li, X. H.; Wang, J. X.; Qi, A. Structure and Electrochemical Performance of $LiCoO_2$ Cathode Material in Different Voltage Ranges. *Ionics* **2014**, *20*, 1525−1534.
(8) Geder, J.; Hoster, H. E.; Jossen, A.; Garche, J.; Yu, D. Y. W. Impact of Active Material Surface Area on Thermal Stability of $LiCoO_2$ Cathode. *J. Power Sources.* **2014**, *257*, 286−292.
(9) Yue, P.; Wang, Z. X.; Peng, W. J.; Li, L. J.; Guo, H. J.; Li, X. H.; Hu, Q. Y.; Zhang, Y. H. Preparation and Electrochemical Properties of Submicron $LiNi_{0.6}Co_{0.2}Mn_{0.2}O_2$ as Cathode Material for Lithium ion Batteries. *Scr. Mater.* **2011**, *65*, 1077−1080.
(10) Nitta, N.; Wu, F. X.; Lee, J. T.; Yushin, G. Li-ion Battery Materials: Present and Future. *Mater. Today.* **2015**, *18*, 252−264.
(11) Padhi, A. K.; Nanjundaswamy, K. S.; Masquelier, C.; Goodenough, J. B. Mapping of Transition Metal Redox Energies in Phosphates with Nasicon Structure by Lithium Intercalation. *J. Electrochem. Soc.* **1997**, *144*, 2581−2586.
(12) Yamada, A.; Chung, S. C.; Hinokuma, K. Optimized $LiFePO_4$ for Lithium Battery Cathodes. *J. Electrochem. Soc.* **2001**, *148*, A224−A229.
(13) Ouyang, C. Y.; Shi, S. Q.; Wang, Z. X.; Huang, X. J.; Chen, L. Q. First-Principles Study of Li Ion Diffusion in $LiFePO_4$. *Phys. Rev. B.* **2004**, *69*, 104303.
(14) Zhang, H.; Tang, Y. H.; Shen, J. Q.; Xin, X. G.; Cui, L. X.; Chen, L. J.; Ouyang, C. Y.; Shi, S. Q.; Chen, L. Q. Antisite Defects and Mg Doping in $LiFePO_4$: A first-Principles Investigation. *Appl. Phys. A: Mater. Sci. Process.* **2011**, *104*, 529−537.
(15) Yuan, L. X.; Wang, Z. H.; Zhang, W. X.; Hu, X. L.; Chen, J. T.; Huang, Y. H.; Goodenough, J. B. Development and Challenges of $LiFePO_4$ Cathode Material for Lithium-ion Batteries. *Energy Environ. Sci.* **2011**, *4*, 269−284.
(16) Deng, S. X.; Wang, H.; Liu, H.; Liu, J. B.; Yan, H. Research Progress in Improving the Rate Performance of $LiFePO_4$ Cathode Materials. *Nano-Micro Lett.* **2014**, *6*, 209−226.
(17) Wang, J. J.; Sun, X. L. Understanding and Recent Development of Carbon Coating on $LiFePO_4$ Cathode Materials for Lithium-ion Batteries. *Energy Environ. Sci.* **2012**, *5*, 5163−5185.
(18) Hwang, B. J.; Tsai, Y. W.; Carlier, D.; Ceder, G. A Combined Computational/Experimental Study on $LiNi_{1/3}Co_{1/3}Mn_{1/3}O_2$. *Chem. Mater.* **2003**, *15*, 3676−3682.
(19) Yabuuchi, N.; Ohzuku, T. Novel Lithium Insertion Material of $LiNi_{1/3}Co_{1/3}Mn_{1/3}O_2$ for Advanced Lithium-ion Batteries. *J. Power Sources* **2003**, *119*, 171−174.
(20) Xiao, J.; Chernova, N. A.; Whittingham, M. S. Influence of Manganese Content on the Performance of $LiNi_{0.9-y}Mn_yCo_{0.1}O_2$ ($0.45 \leq y \leq 0.60$) as a Cathode Material for Li-ion Batteries. *Chem. Mater.* **2010**, *22*, 1180−1185.
(21) Venkateswara Rao, C.; Leela Mohana Reddy, A.; Ishikawa, Y.; Ajayan, P. M. $LiNi_{1/3}Co_{1/3}Mn_{1/3}O_2$-Graphene Composite as a Promising Cathode for Lithium-ion Batteries. *ACS Appl. Mater. Interfaces.* **2011**, *3*, 2966−2972.
(22) Li, Z.; Chernova, N. A.; Roppolo, M.; Upreti, S.; Petersburg, C.; Alamgir, F. M.; Whittingham, M. S. Comparative Study of the Capacity and Rate Capability of $LiNi_yMn_yCo_{1-2y}O_2$ (y = 0.5, 0.45, 0.4, 0.33). *J. Electrochem. Soc.* **2011**, *158*, A516−A522.
(23) Petersburg, C. F.; Li, Z.; Chernova, N. A.; Whittingham, M. S.; Alamgir, F. M. Oxygen and Transition Metal Involvement in the Charge Compensation Mechanism of $LiNi_{1/3}Co_{1/3}Mn_{1/3}O_2$ Cathodes. *J. Mater. Chem.* **2012**, *22*, 19993−20000.
(24) Noh, H. J.; Youn, S.; Yoon, C. S.; Sun, Y. K. Comparison of the Structural and Electrochemical Properties of Layered $Li[Ni_xCo_yMn_z]O_2$ ($x = 1/3$, 0.5, 0.6, 0.7, 0.8 and 0.85) Cathode Material for Lithium-Ion Batteries. *J. Power Sources.* **2013**, *233*, 121−130.
(25) Hu, E.; Yu, X. Q.; Lin, R. Q.; Bi, X. X.; Lu, J.; Bak, S.; Nam, K. W.; Xin, H. L.; Jaye, C.; Fischer, D. A.; et al. Evolution of Redox Couples in Li- and Mn-Rich Cathode Materials and Mitigation of Voltage Fade by Reducing Oxygen Release. *Nat. Energy.* **2018**, *3*, 690−698.
(26) Hou, X. Y.; Ohta, K.; Kimura, Y.; Tamenori, Y.; Tsuruta, K.; Amezawa, K.; Nakamura, T. Lattice Oxygen Instability in Oxide-Based Intercalation Cathodes: A Case Study of Layered $LiNi_{1/3}Co_{1/3}Mn_{1/3}O_2$. *Adv. Energy Mater.* **2021**, *11*, 2101005.
(27) Kuo, L. Y.; Guillon, O.; Kaghazchi, P. On the Origin of Non-Monotonic Variation of the Lattice Parameters of Li-$Ni_{1/3}Co_{1/3}Mn_{1/3}O_2$ with Lithiation/Delithiation: A First-Principles Study. *J. Mater. Chem. A* **2020**, *8*, 13832−13841.
(28) Dudarev, S. L.; Botton, G. A.; Savrasov, S. Y.; Humphreys, C. J.; Sutton, A. P. Electron-Energy-Loss Spectra and the Structural Stability of Nickel Oxide: An LSDA+ *U* Study. *Phys. Rev. B.* **1998**, *57*, 1505−1509.
(29) Kresse, G.; Furthmuller, J. Efficient Iterative Schemes for Ab Initio Total-Energy Calculations Using a Plane-Wave Basis Set. *Phys. Rev. B.* **1996**, *54*, 11169−11186.
(30) Kresse, G.; Joubert, D. From Ultrasoft Pseudopotentials to the Projector Augmented-Wave Method. *Phys. Rev. B.* **1999**, *59*, 1758−1775.
(31) Perdew, J. P.; Burke, K.; Ernzerhof, M. Generalized Gradient Approximation Made Simple. *Phys. Rev. Lett.* **1996**, *77*, 3865−3868.

(32) Zhou, F.; Cococcioni, M.; Marianetti, C. A.; Morgan, D.; Ceder, G. First-Principles Prediction of Redox Potentials in Transition-Metal Compounds with LDA+ *U*. *Phys. Rev. B.* **2004**, *70*, 235121.
(33) Wang, L.; Maxisch, T.; Ceder, G. Oxidation Energies of Transition Metal Oxides within the GGA+*U* Framework. *Phys. Rev. B.* **2006**, *73*, 195107.
(34) Jain, A.; Hautier, G.; Ong, S. P.; Moore, C. J.; Fischer, C. C.; Persson, K. A.; Ceder, G. Formation Enthalpies by Mixing GGA and GG + U Calculations. *Phys. Rev. B.* **2011**, *84*, No. 045115.
(35) Koyama, Y.; Arai, H.; Tanaka, I.; Uchimoto, Y.; Ogumi, Z. Defect Chemistry in Layered $LiMO_2$ (M = Co, Ni, Mn, and $Li_{1/3}Mn_{2/3}$) by First-Principles Calculations. *Chem. Mater.* **2012**, *24*, 3886−3894.
(36) Kim, Y. First-Principles Investigation of the Structural Characteristics of $LiMO_2$ Cathode Materials for Lithium Secondary Batteries. *J. Mol. Struct.* **2015**, *1099*, 317−322.
(37) Koyama, Y.; Tanaka, I.; Adachi, H.; Makimura, Y.; Ohzuku, T. Crystal and Electronic Structures of Superstructural $Li_{1-x}[Co_{1/3}Ni_{1/3}Mn_{1/3}]O_2$ ($0 \leq x \leq 1$). *J. Power Sources.* **2003**, *119−121*, 644−648.
(38) Koyama, Y.; Yabuuchi, N.; Tanaka, I.; Adachi, H.; Ohzuku, T. Solid-State Chemistry and Electrochemistry of $LiNi_{1/3}Co_{1/3}Mn_{1/3}O_2$ for Advanced Lithium-ion Batteries. *J. Electrochem. Soc.* **2004**, *151*, A1545−A1551.
(39) Tsai, Y. W.; Hwang, B. J.; Ceder, G.; Sheu, H. S.; Liu, D. G.; Lee, J. F. In-Situ X-Ray Absorption Spectroscopic Study on Variation of Electronic Transitions and Local Structure of $LiNi_{1/3}Co_{1/3}Mn_{1/3}O_2$ Cathode Material During Electrochemical Cycling. *Chem. Mater.* **2005**, *17*, 3191−3199.
(40) Zheng, F.; Zheng, S. Y.; Zhang, P.; Zhang, X. F.; Wu, S. Q.; Yang, Y.; Zhu, Z. Z. Impact of Structural Transformation on Electrochemical Performances of Li-Rich Cathode Materials: The Case of Li_2RuO_3. *J. Phys. Chem. C.* **2019**, *123*, 13491−13499.
(41) Ohzuku, T.; Makimura, Y. Layered Lithium Insertion Material of $LiNi_{1/3}Co_{1/3}Mn_{1/3}O_2$ for Lithium-Ion Batteries. *Chem. Lett.* **2001**, *30*, 642−643.
(42) Kim, J. M.; Chung, H. T. The First Cycle Characteristics of $Li[Ni_{1/3}Co_{1/3}Mn_{1/3}]O_2$ Charged up to 4.7 V. *Electrochim. Acta* **2004**, *49*, 937−944.
(43) Lee, G. H.; Wu, J. P.; Kim, D.; Cho, K.; Cho, M.; Yang, W. L.; Kang, Y. M. Reversible Anionic Redox Activities in Conventional $LiNi_{1/3}Co_{1/3}Mn_{1/3}O_2$ Cathodes. *Angew Chem Int Ed.* **2020**, *59*, 8681−8688.
(44) Limpijumnong, S.; Van de Walle, C. Diffusivity of Native Defects in Gan. *Phys. Rev. B.* **2004**, *69*, No. 035207.
(45) Ouyang, C. Y.; Šljivančanin, Ž.; Baldereschi, A. First-Principles Study of γ-Al_2O_3(100) Surface. *Phys. Rev. B.* **2009**, *79*, 235410.
(46) Reuter, K.; Scheffler, M. Composition, Structure, and Stability of RuO_2(110) as a Function of Oxygen Pressure. *Phys. Rev. B.* **2001**, *65*, No. 035406.

https://doi.org/10.1021/acsomega.2c00375
ACS Omega 2022, 7, 14875−14886